Nanochemo-mechanical signature of organic-rich shales: a coupled indentation–EDX analysis

Citation: Abedi, Sara et al. "Nanochemo-Mechanical Signature of Organic-Rich Shales: a Coupled indentation–EDX Analysis." Acta Geotechnica 11, 3 (January 2016): 559–572 © 2016 Springer-Verlag Berlin Heidelberg

As Published: http://dx.doi.org/10.1007/S11440-015-0426-4

Publisher: Springer-Verlag

Persistent URL: http://hdl.handle.net/1721.1/117471

Version: Author's final manuscript: final author's manuscript post peer review, without publisher's formatting or copy editing

Nano-Chemomechanical Signature of Organic-Rich Shales: A Coupled Indentation-EDX Analysis

By: Sara Abedi[1,*,**], Mirna Slim[1], Ronny Hofmann[2], Taras Bryndzia[2] and Franz-Josef Ulm[1]

[1] Department of Civil and Environmental Engineering, Massachusetts Institute of Technology, Cambridge, MA.
[2] Shell International Exploration and Production, Projects & Technology, Houston, TX.

Abstract

The organic-inorganic nature of organic-rich source rocks poses several challenges for the development of functional relations that link mechanical properties with geochemical composition. With this focus in mind, we herein propose a method that enables chemo-mechanical characterization of this highly heterogeneous source rock at the micron and submicron length scale through a statistical analysis of a large array of Energy Dispersive X-Ray Spectroscopy (EDX) data coupled with nanoindentation data. The ability to include elemental composition to the indentation probe via EDX is shown to provide a means to identify pure material phases, mixture phases and interfaces between different phases. Employed over a large array, the statistical clustering of this set of chemo-mechanical data provides access to the properties of the fundamental building blocks of clay-dominated organic-rich source rocks. The versatility of the approach is illustrated through the application to a large number of source rocks of different origin, chemical composition and organic content. We find that the identified properties exhibit a unique scaling relation between stiffness and hardness. This suggests that organic-rich shale properties can be reduced to their elementary constituents, with several implications for the development of predictive functional relations between chemical composition and mechanical properties of organic-rich source rocks such as the intimate interplay between clay packing, organic maturity, and mechanical properties of porous clay/organic phase.

Keywords: Organic-rich shale, Nanoindentation, Energy Dispersive X-Ray Spectroscopy, Cluster modeling, Volume fraction, Anisotropy, Ductility

* Corresponding Author: sara.abedi@pe.tamu.edu

** Now at Harold Vance Department of Petroleum Engineering, Texas A&M University, College Station, TX

1. Introduction

Geomaterials such as organic rich shales, can be considered as multiphase and multiscale material systems [17] with intrinsic heterogeneity in chemical composition (including organic diversity (namely maturity) and mineralogy), microtexture and mechanical properties [8]. An improved understanding of fundamental poroelasticity and strength behavior of organic rich shales can lead to development of predictive models that overcome the demand for costly and time-consuming detailed experiments to access their mechanical behavior. For this purpose, it is instructive to explore the complex mechnanical properties of organic rich source rocks at multiple scales, as shown in Figure 1.

Level II corresponds to the characteristic size in the sub-millimeter and millimeter range and is the scale of conventional understanding of organic rich shales regarding their anisotropic poromechanics (Fig. 1). Level I is the scale of porous clay composite intermixed with organic matter. This scale is the scale of nanoindentation and advanced observational methods such as SEM and EDX and is the level of study in this investigation. Level I is of particular importance since porous clay/organic composite is considered as the main driver of macroscopic behavior of organic-rich shales as clay minerals, their packing density, and organic materials control the mechanical and transport properties of these source rocks [3]. Moreover, there is an increasing evidence that maturity of organic matter influences the texture, anisotropy, and ductility of these organic-rich source rocks [46-47]. Finally, level 0 corresponds to the scale of the elementary solid clay particles that make the solid clay phase in organic-rich shales. It should be mentioned that the multi-scale approach followed in this work can be applied to other geomaterials provided that the different scales satisfy the scale separability condition [17].

Following the aforementioned multi-scale structure model and in order to ful-fill the material science paradigm, that is to relate chemical composition, microstructural features, and mechanical performance, the chemo-mechanical properties at fundamental length sacles need to be fully characterized. Advanced characterization techniques have been used to study distinct features of heterogeneous geomaterials at nanometer and micrometer length scales. For instance, valuable insight into the heterogeneity of microstructural features has been obtained by synchrotron x-ray analysis [33, 57-58] small angle neutron scattering [27], and advanced imaging by scanning electron microscopy (SEM) and transmission electron microscopy (TEM) [4, 25, 28]. Similarly, the heterogeneity of mechanical properties has been studied by Atomic force microscopy (AFM) and instrumented indentation on organic-free shale materials [45, 7, 52, 54, 60-61, 3] and organic/inorganic phases in oil and gas bearing shales [2, 39, 59]. Yet, a characterization method that (1) integrates geochemical and mechanical properties in the assessment of organic-rich shale properties, and (2) is able to handle the high heterogeneity of the rock remains to be developed. The method proposed in this paper aims at such a chemo-mechanical characterization of organic-rich shales at micrometer and sub-micrometer length scales (level I) using coupled nanoindentation and energy dispersive x-ray spectroscopy (EDX). The approach herein proposed is an extension to previous approaches developed for inorganic (organic-free) caprocks [12] and cements

[9, 30]. Specifically, the original idea advanced in this investigation is that the extensive data sets obtained by both chemical and mechanical testing techniques at the same location and at similar length scales lend themselves to an effective chemo-mechanical clustering analysis to resolves spatial, chemical and mechanical heterogeneities in the form of chemo-mechanical phases present within the probed region.

The paper is organized as follows: Section 2 presents the studied materials and the different techniques employed for both chemo-mechanical data acquisition (EDX, nanoindentation) and data analysis by means of clustering at micrometer and sub-micrometer length scales of organic-rich source rocks. The results that can be obtained with this coupled indentation-EDX experiments are discussed in details in Section 3 for a mature gas shale (Haynesville). Finally, in Section 4, the versatility of the approach is illustrated through application to a large range of clay-dominated organic-rich source rocks.

Figure 1 goes here

2. Materials and Methods

2.1. Materials

Several organic-rich shale samples from major shale reservoirs of different mineralogy and maturity levels were considered in this study (for mineralogy and Total organic content (TOC), see Table 1); namely Haynesville, Marcellus, Fayetteville , Antrim , and Barnett. Clay minerals in these samples were mostly either illite or mixed illite-smectite, with relatively smaller amounts of kaolinite and chlorite. From Rock-Eval analysis, samples from Haynesville, Marcellus, and Fayetteville were identified as mature gas shale samples, whereas samples from Antrim, and Barnett are immature source rocks. The porosity of the samples was either obtained using Gas Research Institute (GRI) protocols (Haynesville) [35-37], or estimated by comparing the bulk densities with the average mineral densities. Based on the mass fraction of material components reported in Table 1, volume fraction of individual solid constituents of samples are obtained. The volume fraction of a particular material constituent k, is determined by:

$$\eta_k = (1-\phi)\frac{{m_k}/{\rho_k}}{\sum_{i=1}^{N} {m_i}/{\rho_i}} \quad (1)$$

where N represents the number of material phases in the sample, m_i the mass fraction of the solid constituent (Table 1), ρ_i the corresponding mass density (in this study, densities of 2.65-2.82, 2.65, and 2.71 g/cm^3 are considered for clay, quartz and carbonates respectively[Ortega, 2010; www.mindat.org]), and ϕ the porosity obtained experimentally. Table 2 represents the volume fractions of the detected material phases in the studied samples. Clay is the main mineral constituents of these samples with lateral and thickness dimensions of 0.1 - 4 μm and 0.05 - 2 μm; respectively [12, 41]. Regarding the density of organic matter, a variety of values have been used in the literature for organic density, most of which lie in a narrow range. For instance, Mavko et al., [33] has

reported a range of 1.1-1.4 g/cc, whereas Vernik and Landis [55] have used a value of 1.25 g/cc in their calculations. Taking into account these values, a kerogen density of 1.2 g/cc has been assumed in this study.

Table 1 goes here

Table 2 goes here

2.2. Sample Preparation

Sample surface preparation is essential for surface tests such as nanoindentation and EDX. The surface to be tested should be as smooth as possible and parallel with the bottom surface of the sample. Specifically, trimmed samples of 10 mm diameter and 5 mm height were first coarse polished on 400 grit hard perforated pads (TexMet P, Buehler), using an oil-based diamond suspension to prevent chemical reactions. In the next step, samples were dry polished using consecutively 9 μm, 3 μm, and 1 μm aluminum oxide abrasive disks (FibrMet, Buehler). In between polishing steps, the specimens were ultrasonicated in n-decane solution that does not react with the shale minerals, nor with the organic matter. AFM roughness characterization of shale samples prepared with the same procedure showed root-mean-squared (RMS) roughness of 30-150 nm [12, 5]. According to Donnelly et al. (2006), in order to avoid the effects of surface roughness on the results, the obtained indentation depths should be greater than 3 times the RMS roughness (450 nm in this study)

2.3. Grid Nanoindentation Technique

Instrumented grid indentation provides a tool to characterize the mechanical behavior of a heterogeneous material at sub-micrometer length scales. A large set of indentation tests is carried out on a surface. Each test consists of impinging an indenter tip of known geometry (here, a Berkovich tip with equivalent half-cone angle of 70.32° and curvature radius of approximately 30 nm.) and mechanical properties onto the surface of the material of interest [54, 10, 48], and the mechanical properties of the indented bulk material are extracted from the force-displacement curve (*P*-*h* curve, Figure 2) by applying a continuum scale model to obtain the indentation modulus *M*, and the indentation hardness *H*:

$$M = \frac{\sqrt{\pi}}{2}\frac{S}{\sqrt{A_c}} \tag{2}$$

$$H = \frac{P}{A_c} \tag{3}$$

where P is the measured maximum indentation load, $S = \frac{dP}{dh}$ is the measured initial slope of the unloading branch of the *P*-*h* curve, and A_c is the projected area of contact between the indenter tip and sample surface, which is determined as a function of the measured maximum indentation depth, h_{max} [43].

In this work, each indentation test consisted of a linear increasing load to 4.8 mN in 10 s, followed by a 10 holding phase, and a linear unloading in 10 s. Several indentation grids were performed on samples described in Section 2.1. The spacing between indentation points in each grid is between 3 to 6 micrometer, which provides the required separation between indents. Each grid is composed of 400 to 480 tests making the grids cover surfaces of between 60x60 μm^2 to 120x120 μm^2.

Figure 2 goes here

2.4. Energy Dispersive X-Ray Spectroscopy

Energy Dispersive X-Ray Spectroscopy (EDX), a common type of Electron Probe Micro-Analyzer (EPMA) technique, is employed in this study for elemental analysis of organic rich shale samples. The technique utilizes the X-Ray spectrum emitted from the incited solid specimen as a result of a beam of electrons bombarding the sample surface to provide a localized chemical analysis. In EDX, the emitted X-rays are classified based on their energy, and the excited material volume depends on the electron beam energy and material density [23, 49]. One of the most important applications of EDX is elemental mapping which provides spatial distribution of elements of interest over a specific area by collecting X-ray energies of secondary electrons resulting from interaction between an electron beam and a sample. The EPMA technique has been widely used in geology, for instance in the investigation of pore and grain size distributions of individual minerals [40, 31, 15, 50-51].

In order to access quantitative elemental composition maps that might represent atomic weight, atomic fractions, actual weight, or atomic ratios of elements, one needs to perform standard quantification at each pixel of quantitative EDX maps [26, 9]. The ratio of mass concentration of the element of interest between the specimen and the standard material is proportional to the ratio of the intensity of a characteristic X-ray measured from the specimen to that emitted from the standard, with the correction which accounts for matrix effects (ZAF) [23, 42]. The measured peak intensities must also be corrected for background and overlap effects.

Another way of obtaining elemental composition maps by EDX, is to acquire auto-scaled X-ray intensities from the compositional maps which are generally shown in the commercial EDX softwares. Such compositional maps do not represent quantitative local chemistry at indentation points and the auto-scaled intensity values are used as qualitative indicators of a phase [23, 42, 22]. Applying this method in our chemo-mechanical analysis, and given the uniqueness of the elemental chemical composition of each phase in the studied organic-rich shale samples, each phase can be distinctively linked to one composition of auto-scaled intensity values on average.

In this study, EDX maps were acquired with a JEOL JSM-5910 general purpose scanning electron microscope equipped with a Bruker EDX system for elemental analysis. The maps were acquired over the same area on which the nanoindentation grid was performed, and the intensities were averaged around the indentation spots to provide a unique elemental composition for each indentation point on the grid. This elemental analysis was performed with an accelerating voltage of 15 kV, and a working distance of

10 mm. While all major constituents relevant for the characterization of gas shale specimens were acquired over the indentation grid, only a reduced number of elemental intensities are required for proper chemo-mechanical phase identification. For instance, for identification of clay-rich phases, these are the Si and Al elemental intensities.

2.5. Length Scale Compatibility in Coupled EDX – Nanoindentaion Analysis

An important aspect in coupled EDX-nanoindentation is the compatibility of the characteristic length scales of the voxel assessed respectively by EDX and nanoindentation. In EDX, this length scale is governed by the accelerating voltage. For a 15 kV beam voltage, Deirieh et al. (2012) showed from Monte Carlo simulations on common shale constituents such as illite and quartz that such a beam voltage probes elemental intensities at a length scale of L=2~3 μm (Fig. 3). On the other hand, the characteristic voxel size in indentation corresponds approximately to 3-5 times the indentation depth [11, 54]. Thus, in order to probe comparable material volumes by each method, a maximum indentation load of P=4.8 mN was chosen, which leads, for the tested samples, to an average indentation depth of $h_{max} = 400 - 800$ nm. The obtained indentation depths closely satisfy the constraint imposed by surface roughness.

Figure 3 goes here

2.6. Statistical Approach to Indentation and EDX Experiments for Heterogeneous Materials

Natural composite materials are generally very complex, requiring the use of grid indentation and EDX techniques on the material surface. At level I of the organic-rich shales (Fig. 1), the porous clay/organic composite is composed of fine-sized clay particles intermixed with organic matter and nanopores with characteristic length scales d. If the characteristic length of the probed volume l is such that $d<<l$, the chemo-mechanical experiment will sense the on-average homogenized properties of the probed material volume. Moreover, the characteristic length scale of the experiments, l, need to be smaller than the silt-size inclusions $l<<D$ to access the properties of the matrix material and the inclusions. Because of the small-sized clay structures comparing to the probed material volume, the standard EMPA technique can not be used to analyze the exact compositional features of clay particles. The proposed experimental approach can only obtain the on-average porous clay/organic chemo-mechanical properties across different locations on the organic-rich shale matrix.

The analysis of chemo-mechanical properties of such heterogenous material requires the use of statistical analysis of the generated experimental data. In this type of analysis, it is also necessary to acquire a large number of indents in order to avoid sampling effects, which demands the use of an adequately large testing surface comparing to the size of distinct material phases of interest.

A multi-variate cluster modeling approach is used for statistical analysis of the collected mechanical and chemical data. Through this method, one can identify the most likely number of clusters in a data set, as well as the uncertainty of observations belonging to a cluster based on statistical criteria. The cluster modeling considers each event

(comprising nanoindentation and EDX measurements) to be a realization of the random multi-dimensional vector $= (X_i^T, \dots, X_n^T)$, where n is the total number of events (i.e. total number of grid indents). The multi-dimension corresponds to the indentation modulus (M) and hardness (H) as well as chemical components obtained from EDX, which were measured for each of the n tests. The probability density function $f(x_i)$ of the observed data x_i in X_i in a G-component mixture is:

$$f(x_i, \Psi) = \sum_{k=1}^{G} \tau_k \, \phi(x_i, \mu_k, \sum_k) \tag{4}$$

where τ_k is the probability that an observation belongs to the k-th component ($\sum_{k=1}^{G} \tau_k = 1$), $\Psi = (\tau_1, \dots, \tau_k, \xi^T)^T$ with ξ containing the (unknown) group mean, μ_k, and the covariance matrix, Σ_k, and $\phi(x_i, \mu_k, \Sigma_k)$ corresponding to the multi-variate normal density:

$$\phi(x_i, \mu_k, \Sigma_k) = \frac{exp\left(-\frac{1}{2}(x_i - \mu_k)^T (\Sigma_k)^{-1}(x_i - \mu_k)\right)}{\sqrt{det\ (2\pi\Sigma_k)}} \tag{5}$$

The best model is obtained by fitting models with differing parameterization and/or number of components to the data by maximum likelihood, and then by implementing a statistical criterion for model selection, here the Bayesian Information Criteria, BIC. The reader is referred to [19-21] for a detailed discussion of clustering analysis. In this study, the open source R package Mclust (http://www.stat.washington.edu/ mclust), well suited for normal mixture modeling and model-based clustering, was employed. The package provides functions for mixture modeling and implements maximum likelihood estimation and Bayesian Information Criteria (BIC) to identify the most likely model and the number of clusters.

3. Results

3.1. Coupled EDX-Grid Nanoindentation Technique

To illustrate the added value of enriching mechanical data by chemical data for a statistical phase identification, a comparison of cluster analysis obtained respectively without (Fig. 4) and with (Fig. 5) the EDX analysis is of interest. This comparison is illustrated in Figures 4-6 for one grid on Haynesville shale, but similar results were obtained for other grids and other shale rocks as well. Specifically, while the pure mechanical clustering (Fig. 4) identifies only two phases, the coupled chemo-mechanical clustering picks up four phases of distinct chemo-mechanical properties. The difference in number of phases and properties is recognized from a comparison of the phase maps shown in Figure 6. In contrast to the pure mechanical phases (Fig. 6a), the coupling with chemistry allows one to distinguish bulk phases from mixture phases (Fig. 6b). In particular, by incorporating maps of “Si” and “Al” from EDX into the clustering analysis, phase 1 is identified as a “clay-rich” phase. Similarly, incorporating ‘Ca’ maps in the

clustering provides a means to identify phases 3 and 4 as "calcite-rich" and "quartz-rich" phases, respectively; whereas phase 2 is identified as a mixture phase at the interface between clay-rich and calcite-rich regions. Thus far, the coupled EDX-grid indentation technique provides a means to match mineralogy with mechanical stiffness and strength properties. It is, however, emphasized, that the coupled chemo-mechanical approach only accounts for inorganic elements. That is, the phases thus identified will certainly include the organic phases as well.

Figure 4 goes here

Figure 5 goes here

Figure 6 goes here

3.2 Comparison with Bulk Mineralogy

The clustering algorithm also provides volume fractions of the clay-rich and calcite-rich regions on a grid. It should be noted, however, that due to the heterogeneity of the sample a single grid size of 60x60 μm^2 to 120x120 μm^2 may not be representative of the bulk mineralogy, and that several grids are typically required for the volume fractions to converge toward the bulk mineralogy. This is shown in Figure 7: As the number of tests increases, the volume fractions converge toward the volume fraction of the clay-rich phase determined from bulk mineralogy. Figure 7 represents the results of chemo-mechanical clustering analysis on 17 grids performed on Haynesville samples. From these 17 grids, we randomly draw, without replacement, the volume fraction of clay rich phase of one grid and average these values as the number of grids increased. The procedure was repeated 100 times and the results are presented in Figure 7. As expected, all runs converge to the average volume fraction of the clay rich phases among all 17 grids of 43% - a value that needs to be compared with the value available from mineralogy. For this comparison, it should be noted that the phases identified from the chemo-mechanical clustering also include porosity and kerogen. Thus for the sought comparison, the bulk mineralogy (in volume%) needs to be corrected to account for both.

To this end, we consider (1) that the porosity is distributed homogeneously in all phases composing the sample, thus considering porosity in both the organic and the inorganic phase; and (2) that the organic matter is mostly concentrated in the clay phase [56, 32, 18] (Figure 8, Table 3 presents volume fraction of kerogen in the clay-rich phase for all samples). These assumptions are built on the multiscale model proposed in Figure 1. The first assumption provides a means to assess the volume fractions of porous clay and kerogen (in e.g. Haynesville samples) by dividing the volume percentage of bulk clay and kerogen (Table 2) by the solid volume fraction, $1-\phi$. For the considered Haynesville samples this provides an average volume fraction of 39% and 6% for the porous clay phase and porous kerogen phase, respectively. The second assumption allows us to simply sum up these two volume fractions, to obtain a total volume fraction of the porous clay/kerogen composite in Haynesville samples of 45%. The value so obtained from mineralogy and porosity measurements compares fairly well with the volume fraction of

the clay-rich phases identified by coupled Nanoindentation and EDX of 43%. The successful comparison not only validates our conjecture that the coupled Nanoindentation-EDX method provides a quantitative means to separate chemo-mechanical phases in organic-rich shales. It also supports our hypotheses regarding the distributions of porosity and organic matter in the microstructure of mature samples; namely a self-consistent porosity distribution throughout the system (i.e. same porosity in all phases), and a kerogen phase spatially correlated with the clay phase. This observation is also consistent with observation made by others that showed both an inter-organic porosity and a mineral porosity [29, 34].

Figure 7 goes here

Figure 8 goes here

Table 3 goes here

4. Discussion: The Elementary Building Block of Organic-Rich Source Rocks

With the coupled chemo-mechanical experimental method thus in place, it is of interest to extend the analysis to a larger set of organic-rich source rocks, ranging from mature to immature samples. Specifically, we herein address the question of whether the clay-rich phase in different source rocks exhibits some chemo-mechanical functional relations that link mechanical properties to mineralogy, packing fractions and maturity. With this objective in mind, several nanoindentation grids in orthogonal directions were conducted on organic-rich samples described in section 2.1, with X1 and X3 corresponding to the parallel-to-bedding and normal-to-bedding direction, respectively. The porous clay/kerogen phases were identified for each direction (X1 and X3) by the described coupled nanoindentation-EDX techniques.

Figures 9 and 10 summarize the indentation results of the porous clay/kerogen phases of the studied samples, in the form of a plot of the mean indentation modulus vs. indentation hardness (Fig. 8), and of (M, H) vs. the clay packing density , $\eta_c = 1 - (\eta_k + \phi)$ (where ϕ is the porosity and η_k is the kerogen volume fraction) and the kerogen volume fraction, η_k (Fig. 9), respectively. The results are also provided in Table 4. The following observations deserve attention:

1. The stiffness and hardness values of the clay-rich phases of different formations exhibit –on first order– a power scaling of the form $M \sim H^{\alpha}$ (Fig. 8), where $\alpha < 1$. This scaling is of some significance if we remind ourselves that the results presented in Figure 9 are obtained from samples with different maturity, total organic content (TOC) (Table 2), and porosity (Table 1). Such a distinct scaling relation is a hallmark of functional relations between (M, H) and microtexture quantities, such as clay packing density and kerogen content.

2. The clay-rich phase exhibits a distinct anisotropy in both stiffness (M) and strength-hardness (H), as values in the X1 direction are typically greater than

values in the X3-direction [14]. Specifically, the elastic anisotropy, M_1/M_3 (where M_1 and M_3 represent the indentation modulus in X1 and X3 directions, respectively), appears to increase with the clay packing fraction (Fig. 9a), but seems unaffected by the kerogen volume fraction (Fig. 9c). This type of elastic anisotropy is reminiscent of that of organic-free clay-bearing shale materials [52, 7], and confirms the idea of an effective chemo-mechanical isolation of the clay-rich phase by the suggested method. On the other hand, the indentation hardness (H) which relates to cohesion and friction of the elementary particles [6] is found to be less affected by the clay packing (Fig. 9b), but strongly affected by the kerogen content. In fact, as the kerogen content increases the difference in hardness in the orthogonal direction decreases (Fig. 9d); in stark contrast to the elastic anisotropy (Fig. 9c). That is, while the micron-scale elasticity scales in first-order with the clay packing, the strength behavior appears to be strongly dependent on the kerogen volume fraction in organic-rich clay-bearing source rocks.

The two distinct observations merit further exploration. We thus consider another, yet related, quantity: the ratio of indentation modulus over hardness (M/H). For an elastic material, M/H only depends on the indenter geometry, and equals $M/H = 2tan\theta = 5.6$ for the Berkovich tip of equivalent half-cone angle θ=70.32° employed in our investigation (for derivation see [11]). Greater values of M/H are indicative of the occurrence of plastic deformation mechanisms, as M/H is homogeneous to the inverse of a yield strain. As such, it is commonly employed, in materials science investigations, as a measure of the ductility (see, for instance, Abdolhosseini Qomi et al., [1]). In Figure 11 we thus plot this ductility measure (M/H) as a function of the clay packing (Fig. 11a) and the kerogen content (Fig. 11b). Two competing trends are apparent in these figures; namely (1) a decrease in ductility with decreasing clay packing (Fig. 11a), and (2) an increase in ductility with increasing kerogen content (Fig. 11b). As kerogen volume fraction increases, the ductility also increases till the point that the effect of clay packing density prevails which is a decrease in ductility as clay packing density decreases. This added ductility of the kerogen in an otherwise tightly-packed brittle clay matrix [24], is expected to be more pronounced in immature systems than in mature systems, and appears to us at the origin of the intimate interplay between the organic-inorganic strength-stiffness behavior.

Figure 9 goes here

Figure 10 goes here

Figure 11 goes here

Table 4 goes here

5. Conclusion

The novel methodology of coupled statistical nanoindentation-EDX clustering analysis herein proposed provides an effective means to isolate different chemo-mechanical phases and their interfaces in organic-rich source rocks at micro-meter and sub-micron scale. The method is based on adding relevant chemical markers to mechanical information in a statistical clustering analysis. If carried out over statistically representative surface areas, the method is capable of providing volume fractions of different material constituents.

The overall picture that emerges from the application of the method to a large array of both mature and immature organic-rich rocks of different porosities, is that the clay-rich phase exhibits a unique scaling relation between stiffness (M) and hardness (H). From exploring correlations between mechanical phase properties and clay packing and kerogen content, it appears to us that this scaling is due to an intimate interplay between the increase in elasticity content with clay packing, and a decrease of strength due to the added ductility of kerogen related to an increase in TOC. While this intimate interplay between clay packing and kerogen maturity still merits further investigation, as evidenced by others [47], and corroborated by our own investigation of mature and immature samples, the method here proposed may turn out invaluable for future investigations that aim at reducing the complexity of organic-rich shales to their elementary constituents, with several implications for the development of predictive functional relations between chemical composition and mechanical properties of organic-rich source rocks.

5. Acknowledgment

This work was conducted as part of the X-Shale project, an industry-academia partnership between MIT, Shell and Schlumberger enabled through MIT's Energy Initiative. Shell and Schlumberger provided all the samples used in this study. The experimental results were obtained at X-Hub lab at MIT: https://cshub.mit.edu. The data supporting Figures 9, 10, and 11 are available in Tables 1-4. The authors are grateful to Dr. Nicola Ferralis from MIT for fruitful discussions.

7. References

1. Abdolhosseini Qomi, M.J., Krakowiak, K.J., Bauchy, M., Stewart, K.L., Shahsavari, R., Jagannathan, D., Brommer, D.B., Baronnet, A., Buehler, M.J., Yip, S., Ulm, F.-J., Van Vliet, K.J., and Pellenq, R.J-.M. (2014) “Combinatorial molecular optimization of cement hydrates.” Nature Communications 5, Article number: 4960, doi:10.1038/ncomms5960

2. Ahmadov, R., Vanorio, T., Mavko, G. (2009) "Confocal laser scanning and atomic-force microscopy in estimation of elastic properties of the organic-rich Bazhenov formation. " Leading Edge Vol. 28(1): 18–23, doi: 10.1190/1.3064141

3. Bennett, KC., Berla, LA., Nix, WD., Borja, RI. (2015) “Instrumented nanoindentation and 3D mechanistic modeling of a shale at multiple scales.” Acta Geotechnica Vol. 10 (1): 1-14.

4. Bennett, RH., O'Brien, NR., Hulbert, MH. (1991) "Determinants of clay and shale microfabric signatures: processes and mechanisms. " In: Bennet, RH., O'Brien, NR., Hulbert, MH. (eds) "Microstructure of fine grained sediments: from mud to shale. " Springer, New York, pp 5–32

5. Bobko, C. P. (2008) "Assessing the mechanical microstructure of shale by nanoindentation: The Link between mineral composition and mechanical properties." PhD dissertation, Massachusetts Institute of Technology, Cambridge.

6. Bobko, C. P., Gathier, B., Ortega, J. A., Ulm, F-J., Borges, L., Abousleiman, YN. (2011) "The nanogranular origin of friction and cohesion in shale—a strength homogenization approach to interpretation of nanoindentation results." International Journal of Numerical and Analytical Methods in Geomechanics Vol. 35(17): 1854-1876, doi: 10.1002/nag.984

7. Bobko, C., Ulm, F-J. (2008) "The nano-mechanical morphology of shale. " Mechanics of Materials, Vol. 40(4–5): 318–337, doi:10.1016/j.mechmat.2007.09.006

8. Bustin, R. M. (2012) "Shale gas and shale oil petrology and petrophysics" International Journal of Coal Geology, Vol. 103: 1-2, doi:10.1016/j.coal.2012.09.003

9. Chen, J. J., Sorelli, L., Vandamme, M., Ulm, F-J., Chanvillard, G. (2010) "A coupled nanoindentation/SEM-EDS study on low water/cement ratio portland cement paste: evidence for C–S–H/$Ca(OH)_2$ nanocomposites" Journal of American Ceramic Society, Vol. 93(5): 1484-1493, doi: 10.1111/j.1551-2916.2009.03599.x

10. Constantinides, G., Ravi Chandran, K. S., Ulm, F-J., Van Vliet, K. J. (2006) "Grid indentation analysis of composite microstructure and mechanics: Principles and validation" Materials Science and Engineering A, Vol. 430: 189–202, doi:10.1016/j.msea.2006.05.125

11. Constantinides, G., Ulm, F-J. (2007) "The nanogranular nature of C-S-H" Journal of the Mechanics and Physics of Solids. Vol. 55 (1): 64-90, doi:10.1016/j.jmps.2006.06.003

12. Deirieh, A. (2011) "Statistical Nano-Chemo-Mechanical Assessment of Shale by Wave Dispersive Spectroscopy and Nanoindentation" S. M. dissertation, Massachusetts Institute of Technology, Cambridge.

13. Deirieh, A., Ortega, J. A., Ulm, F.-J., and Abousleiman, Y. (2012) "Nanochemomechanical assessment of shale: a coupled WDS-indentation analysis" Acta Geotechnica, 7, 271-295, doi: 10.1007/s11440-012-0185-4

14. Delafargue A, and Ulm, F.-J. (2004) "Explicit approximations of the indentation modulus of elastically orthotropic solids for conical indentation" Int. J. Solids & Structures 41, 7351-7360, doi:10.1016/j.ijsolstr.2004.06.019

15. Dilks, A., Graham, SC. (1985) “Quantitative mineralogical characterization of sandstones by back-scattered electron image analysis. “Journal of Sedimentary Petrology Vol. 55(3): 347–355, doi: 10.1306/212F86C5-2B24-11D7-8648000102C1865D

16. Donnelly, E., Baker, S.P., Boskey, A.L., van der Meulen, M.C.H. (2006) “Effects of surface roughness and maximum load on the mechanical properties of cancellous bone measured by nanoindentation.” Journal of Biomedical Materials Research A, Vol. 77 (2): 426–435.

17. Dormieux, L., Kondo, D., & Ulm, F.-J. (2006). “Microporomechanics.” Chichester UK: J. Wiley & Sons, doi: 10.1002/0470032006

18. Fitzgerald, JJ., Hamza, AI., Bronnimann, CE., Dec, SF. (1989) “Solid-state 27 Al and 29 Si NMR studies of the reactivity of the aluminum-containing clay mineral kaolinite” Solid State Ionics, Vol. 32–33, Part 1: 378-388

19. Fraley, C., and Raftery, A.E. (1999) “MCLUST: Software for model-based cluster analysis” Journal of Classification, vol. 16: 297-306, doi: 10.1007/s003579900058

20. Fraley, C., and Raftery, A.E. (2002) “Model-based clustering, discriminant analysis, and density estimation” Journal of the American Statistical Association, vol. 97: 611-631, doi:10.1198/016214502760047131

21. Fraley, C., and Raftery, A.E. (2007) “Model-based methods of classification: using the mclust software in chemometrics” Journal of Statistical Software, vol. 18: 1-13, doi:10.1360/jos180001

22. Friel, JJ., Lyman, ChE. (2006) “X-ray mapping in electron-beam instruments” Microscopy and Microanalysis Vol. 12(1): 2–25, doi: 10.1017/S1431927606060211

23. Goldstein, J., Newbury, DE., Joy, D., Lyman, Ch., Echlin, P., Lifshin, E., Sawyer, L., Michael, J. (2007) “Scanning Electron Microscopy and X-ray Microanalysis” 3rd ed. Springer

24. Hantal, G., Brochard, B., Laubie, H., Ebrahimi, D., Pellenq, R.J.-M., Ulm, F.-J., Coasne, B. (2014) “Atomic-scale modelling of elastic and failure properties of clays.” Molecular Physics 112, 1294-1305, doi:10.1080/00268976.2014.897393

25. Hornby, BE., Schwartz, LM., Hudson, JA. (1994) "Anisotropic effective-medium modeling of the elastic properties of shales. " Geophysics Vol. 59(10): 1570–1583, doi:10.1190/1.1443546

26. Hughes, JJ., Trtik, P. (2004) “Micro-mechanical properties of cement paste measured by depth-sensing nanoindentation: a preliminary correlation of physical properties with

phase type" Materials Characterization Vol. 53(2-4) 223–231, doi:10.1016/j.matchar.2004.08.014

27. Jin, L., Rother, G., Cole, DR., Mildner, DFR., Duffy, CJ., Brantley, SL. (2011) "Characterization of deep weathering and nanoporosity development in shale—a neutron study". American Mineralogist Vol. 96(4): 498–512, doi: 10.2138/am.2011.3598

28. Keller, LM., Holzer, L., Wepf, R., Gasser, P. (2011) "3D geometry and topology of pore pathways in Opalinus clay: Implications for mass transport. " Apllied Clay Sciences Vol. 52(1–2): 85–95, doi:10.1016/j.clay.2011.02.003

29. King, H. E., Eberle, A. P. R., Walters, C. C., Kliewer, C. E., Ertas, D., Huynh, C. (2015) "Pore architecture and connectivity in gas shale" Energy Fuels, Vol. 29: 1375 – 1390.

30. Krakowiak, K., Wilson, W., James, S., Musso, S., Ulm F.-J. (2015) "Inference of the phase-to-mechanical property link via coupled X-ray spectrometry and indentation analysis: Application to cement-based materials." Cement and Concrete Research 67, 271-285, doi:10.1016/j.cemconres.2014.09.001

31. Krinsley, DH. (1998) "Back-scattered scanning electron microscopy and image analysis of sediments and sedimentary rocks. " Cambridge University Press, Cambridge

32. Kuila, U., McCarty, DK., Derkowski, A., Fischer, TB., Topór, T., Prasad, M. (2014) "Nano-scale texture and porosity of organic matter and clay minerals in organic-rich mudrocks." Fuel Vol. 135: 359–373, doi:10.1016/j.fuel.2014.06.036

33. Lonardelli, I., Wenk, H-R., Ren, Y. (2007). "Preferred orientation and elastic anisotropy in shales. " Geophysics Vol. 72(2): D33–D40, doi: 10.1190/1.2435966

34. Loucks, RG., Reed, RM., Ruppel, SC., & Hammes, U. (2012) "Spectrum of pore types and networks in mudrocks and a descriptive classification for matrix-related mudrock pores" AAPG Bulletin, Vol.96 (6): 1071–1098.

35. Luffel, D., Guidry, F. (1989). "Core analysis results Comprehensive Study Wells Devonian Shales: Topical Report July 1989" Technical Report Restech Houston, Inc.

36. Luffel, DL., Guidry, FK. (1992). "New core analysis methods for measuring reservoir rock properties of Devonian shale" Journal of Petroleum Technology, Vol. 44(11) : 1184–1190, doi: 10.2118/20571-PA

37. Luffel, DL., Guidry, F. K., Curtis, JB. (1992). "Evaluation of Devonian shale with new core and log analysis methods" Journal of Petroleum Technology, Vol. 44(11) :1192–1197, doi: 10.2118/21297-PA

38. Mavko, G., Mukerji, T., Dvorkin, J.(2009). “Rock Physics Handbook: Tools for Seismic Analysis in Porous media” Cambridge University Press.

39. Mba, K., Prasad, M., Batzle, M. (2010) "The maturity of organic-rich shales using microimpedance analysis. " SPE annual technical conference and exhibition, Florence, September 19–22, SPE 135569, DOI: 10.2118/135569-MS

40. McGee, JJ., Keil, K. (2001) “Application of electron probe microanalysis to the study of geological and planetary materials. “Microscopy and Microanalysis Vol. 7(02): 200–210

41. Mitchell, JK. (2005) “Fundamentals of Soil Behavior”, 3rd ed. Hoboken, N.J: John Wiley & Sons.

42. Newbury, DE., Bright, DS. (1999) “Logarithmic 3-band color encoding: a robust method for display and comparison of compositional maps in electron probe X-ray microanalysis” Microscopy and microanalysis Vol. 5(5): 333–343, doi: 10.1017/S1431927699000161

43. Oliver, WC., Pharr, GM. (2004) “Measurement of hardness and elastic modulus by instrumented indentation: advances in understanding and refinements to methodology” Journal of Materials Research Vol. 19(1): 3–20, doi: 10.1557/jmr.2004.19.1.3

44. Ortega, JA. (2010) “Microporomechanical modeling of shale.” PhD dissertation, Massachusetts Institute of Technology, Cambridge.

45. Prasad, M., Kopycinska, M., Rabe, U., Arnold, W. (2002) "Measurement of Young’s modulus of clay minerals using atomic force acoustic microscopy. " Geophysical Research Letters Vol. 29(8): 13-1–13-4, doi:10.1029/2001GL014054

46. Prasad, M., Mukerji, T. (2003) “Analysis of Microstructural Textures And Wave Propagation Characteristics In Shales” SEG Annual Meeting, 26-31 October, Dallas, Texas.

47. Prasad, M., Mukerji, T., Reinstaedler, M., Arnold, W. (2009) “Acoustic signatures, impedance microstructure, textural scales, and anisotropy of kerogen-rich shales” SPE Annual Technical Conference and Exhibition, 4-7 October, New Orleans, Louisiana, doi:10.2118/124840-MS

48. Randall, NX., Vandamme, M., Ulm, F-J. (2009) “Nanoindentation analysis as a two-dimensional tool for mapping the mechanical properties of complex surfaces” Materials Research Society Vol. 24(3), 679–690, doi: 10.1557/jmr.2009.0149

49. Reed, SJB. (2006) “Electron microprobe analysis and scanning electron microscopy in geology“ 2nd edn. Cambridge University Press, Cambridge

50. Tovey, NK., Krinsley, DH. (1991) “Mineralogical mapping of scanning electron micrographs.“ Sedimentary Geology Vol. 75(1–2): 109–123, doi:10.1016/0037-0738(91)90053-G

51. Tovey, NK., Krinsley, DH., Dent, DL., Corbett, WM. (1992) “Techniques to quantitatively study the microfabric of soils. “ Geoderma Vol. 53(3–4): 217–235, doi:10.1016/0016-7061(92)90056-D

52. Ulm, F-J., Abousleiman, Y. (2006) "The nanogranular nature of shale. " Acta Geotechnica Vol. 1(2): 77–88, doi: 10.1007/s11440-006-0009-5

53. Ulm, F-J., Delafargue, A., Constantinides, G. (2005) "Experimental microporomechanics. " In: Dormieux, L., Ulm, F-J. (eds) "Applied micromechanics of porous materials. " Springer, Wien, pp 207–288

54. Ulm, F-J., Vandamme, M., Bobko, C. P., Ortega, J. A., Tai, K., Ortiz, C. (2007) “Statistical Indentation Techniques for Hydrated Nanocomposites: Concrete, Bone, and Shale. ” Journal of American Ceramic Society Vol. 90(9): 2677-2692, doi:10.1111/j.1551-2916.2007.02012.x

55. Vernik, L., Landis, C. (1996). “Elastic anisotropy of source rocks: Implications for hydrocarbon generation and primary migration” AAPG Bulletin, Vol. 80(4): 531– 544

56. Vernik, L., and Nur, A. (1992) “Ultrasonic velocity and anisotropy of hydrocar- bon source rocks” Geophysics, Vol. 57: 727–735.

57. Voltolini, M., Wenk, H-R., Mondol, NH., Bjorlykke, K., Jahren, J. (2009) "Anisotropy of experimentally compressed kaolinite–illite–quartz mixtures.” Geophysics Vol. 74(1): D13–D23, doi:10.1190/1.3002557

58. World Energy Council. (2007) "Survey of energy resources. Technical report. " World Energy Council

59. Zargari, S., Prasad, M., Mba, K., Mattson, E. (2011) "Organic maturity, hydrous pyrolysis, and elastic property in shales. " Canadian unconventional resources conference, Calgary, November 15–17, SPE 149403, doi: 10.2118/149403-MS

60. Zhang, G., Wei, Z., Ferrell, RE. (2009) "Elastic modulus and hardness of muscovite and rectorite determined by nanoindentation. " Apllied Clay Sciences Vol. 43(2): 271–281, doi:10.1016/j.clay.2008.08.010

61. Zhang, G., Wei, Z., Ferrell, RE., Guggenheim, S., Cygan, RT., Luo, J. (2010) "Evaluation of the elasticity normal to the basal plane of non-expandable 2:1 phyllosilicate minerals by nanoindentation. " American Mineralogist Vol. 95(5–6): 863–869, doi: 10.2138/am.2010.3398

Figures:

Figure 1. Multiscale structure-model of organic-rich shale. Level 0 corresponds to the scale of elementary clay particles at nanometer length scales. Level I is a porous clay/kerogen composite at the scale of micrometer (scale of indentation and advanced observational methods such as SEM and EDX), with the porosity representing the mesoporosity. Level II is the scale of porous organic/inorganic hard inclusion composite.

Figure 2. A typical load versus depth curve obtained by nanoindentation on an organic-rich shale. The indentation hardness, H, and indentation modulus, M, are obtained from the curve.

Figure 3. Monte Carlo simulation (run on CASINO) displaying electron trajectories in EPMA experiment [13]. The trajectories represented by red color (reaching to 0.5 microns of depth) are mostly back-scattered electrons. Trajectories beyond 0.5 are related to low and high energies.

Figure 4. (a) Clustering analysis of grid indentation data (*M,H*) only. Phase 1 and 2 represent active mechanical phases. (b) Plots showing the mean mechanical properties and volume fractions of each of the identified phases [Haynesville].

Figure 5. (a) Chemo-mechanical phase identification from the clustering analysis incorporating both chemical data (Si, Al) and mechanical data (M,H). (b) Plots showing the mean mechanical properties and auto-scaled elemental intensities of the 2 chemical elements (used in clustering) in each of the identified phases [Haynesville]. Phase 1 is identified as a "clay-rich" phase. Similarly, phases 3 and 4 are identified as "calcite-rich" and "quartz-rich" phases, respectively; whereas phase 2 is classified as a mixture phase at the interface between clay-rich and calcite-rich regions.

Figure 6. (a) Grid spatial distribution of different material phases detected by clustering analysis of just mechanical data from indentation. White cells represent points with irregular nanoindentation response which are not considered in the analysis. (b) Spatial distribution of different material phases detected by clustering analysis, incorporating both the chemical and mechanical data. [Haynesville].

Figure 7. Average volume fraction of clay-rich phase as a function of number of grids. The dashed red line represents the average of all 17 grids.

Figure 8. SEM images of Haynesville shale sample at two different magnifications showing the distribution of kerogen in the clay phase.

Figure 9. Mean phase properties of clay/kerogen-rich phase: Indentation modulus versus hardness. Haynesville, Marcellus and Fayetteville samples are mature samples, whereas Barnett and Antrim are immature samples. X1 and X3 stand for indentation into the bedding plane and normal-to-bedding plane, respectively.

Figure 10. Functional relations between mechanical phase properties (M, H) and (a-b) clay packing density. (c-d) kerogen volume fraction. The kerogen volume fraction η_k was determined from TOC, assuming a constant kerogen density of $\rho_k = 1.2$ g/cc and considering that organic matter is mainly concentrated in the clay phase; whereas the clay packing density was obtained from $\eta_c = 1 - (\eta_k + \phi)$, where ϕ is the porosity. Trend lines are to guide the eyes.

Figure 11. Indentation-modulus-to-hardness ratio vs (a) clay packing, and (b) kerogen content. The kerogen volume fraction η_k was determined from TOC, assuming a constant kerogen density of $\rho_k = 1.2$ g/cc and considering that organic matter is mainly concentrated in the clay phase; whereas the clay packing density was obtained from $\eta_c = 1 - (\eta_k + \phi)$, where ϕ is the porosity. The inlet shows the crossplot of η_k vs. η_c. Trend lines are to guide the eyes. X1 and X3 stand for indentation into the bedding plane and normal-to-bedding plane, respectively.

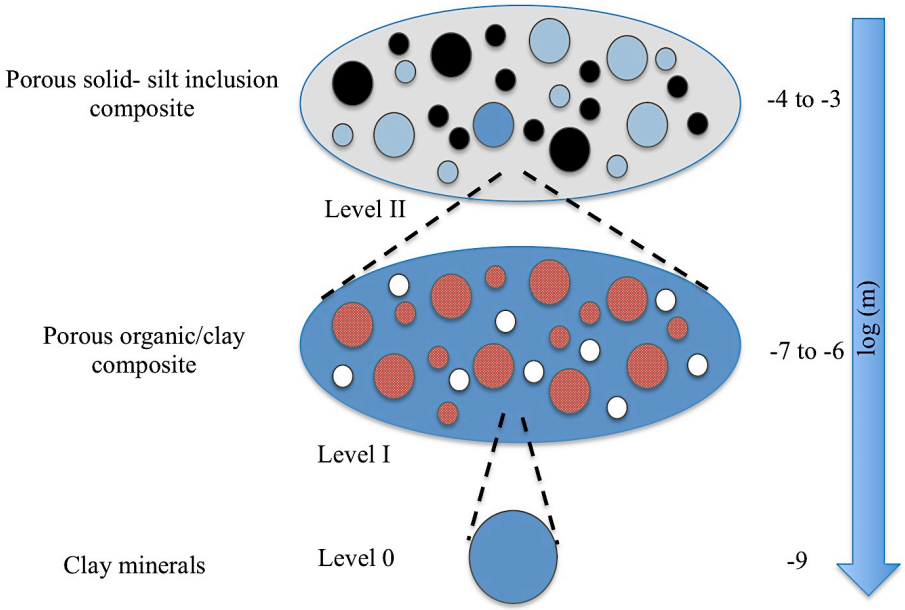

Figure 1. Multiscale structure-model of organic-rich shale. Level 0 corresponds to the scale of elementary clay particles at nanometer length scales. Level I is a porous clay/kerogen composite at the scale of micrometer (scale of indentation and advanced observational methods such as SEM and EDX), with the porosity representing the mesoporosity. Level II is the scale of porous organic/inorganic hard inclusion composite.

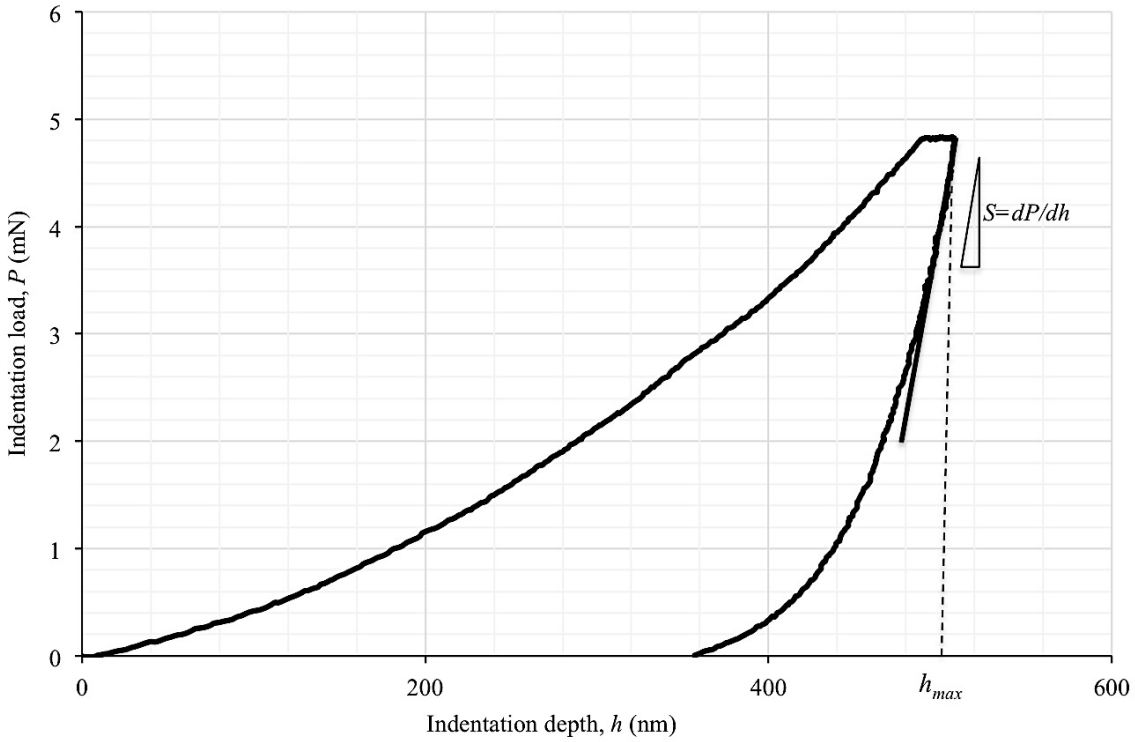

Figure 2. A typical load versus depth curve obtained by nanoindentation on an organic-rich shale. The indentation hardness, H, and indentation modulus, M, are obtained from the curve.

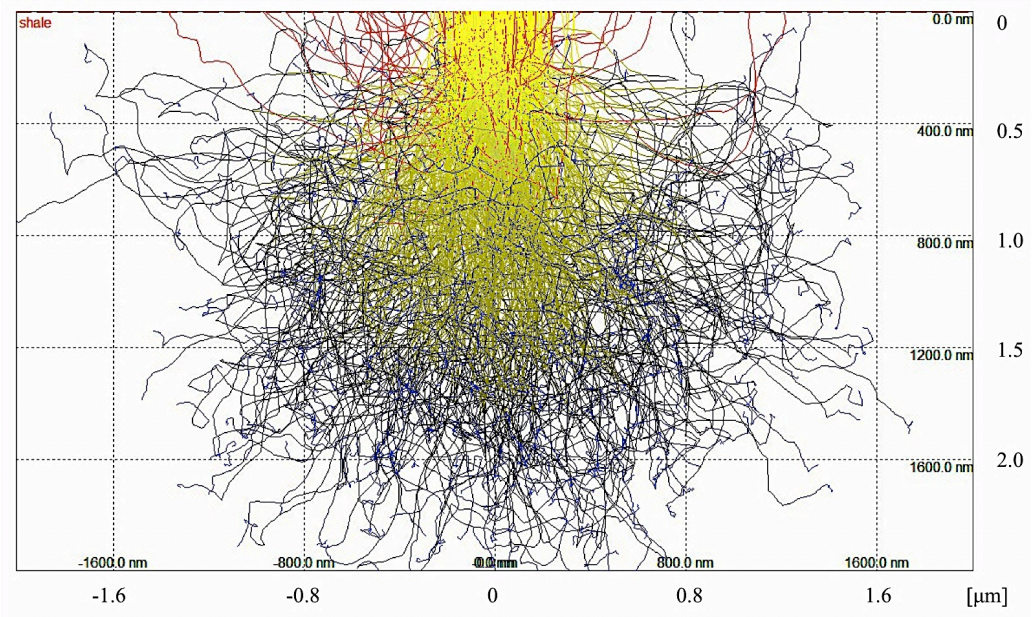

Figure 3. Monte Carlo simulation (run on CASINO) displaying electron trajectories in EPMA experiment [13]. The trajectories represented by red color (reaching to 0.5 microns of depth) are mostly back-scattered electrons. Trajectories beyond 0.5 are related to low and high energies.

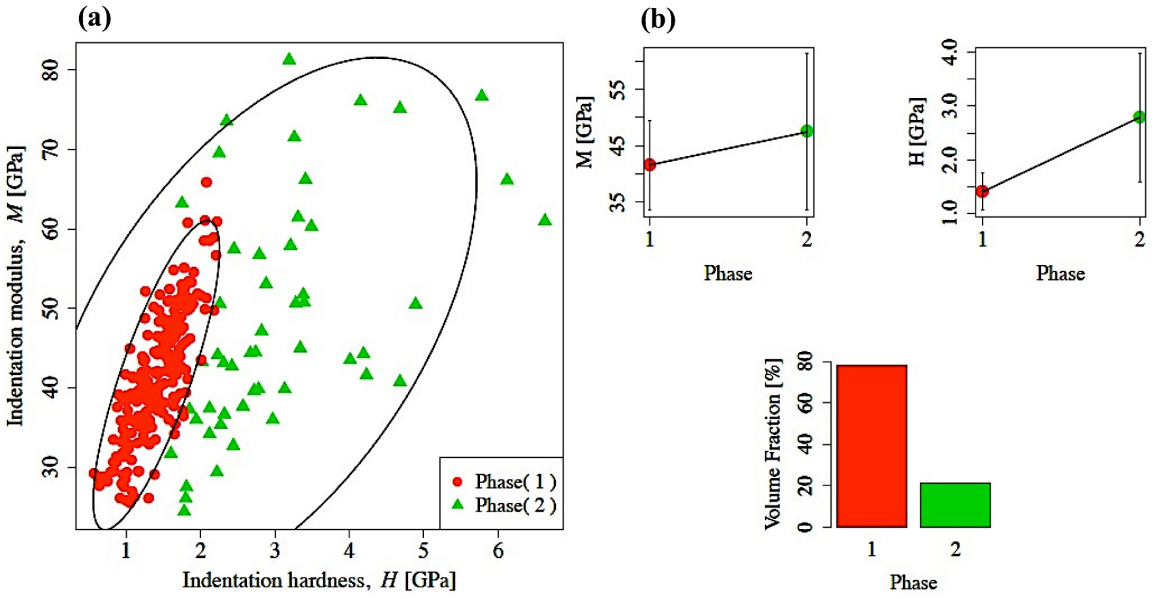

Figure 4. (a) Clustering analysis of grid indentation data (*M,H*) only. Phase 1 and 2 represent active mechanical phases. (b) Plots showing the mean mechanical properties and volume fractions of each of the identified phases [Haynesville].

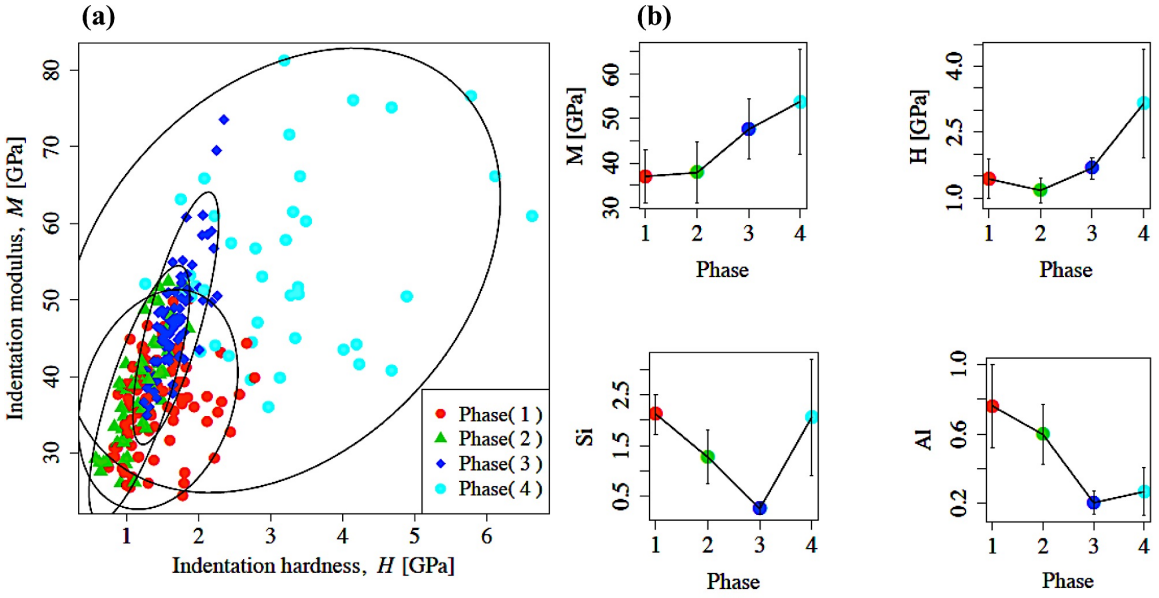

Figure 5. (a) Chemo-mechanical phase identification from the clustering analysis incorporating both chemical data (Si, Al) and mechanical data (*M,H*). (b) Plots showing the mean mechanical properties and auto-scaled elemental intensities of the 2 chemical elements (used in clustering) in each of the identified phases [Haynesville]. Phase 1 is identified as a "clay-rich" phase. Similarly, phases 3 and 4 are identified as "calcite-rich" and "quartz-rich" phases, respectively; whereas phase 2 is classified as a mixture phase at the interface between clay-rich and calcite-rich regions.

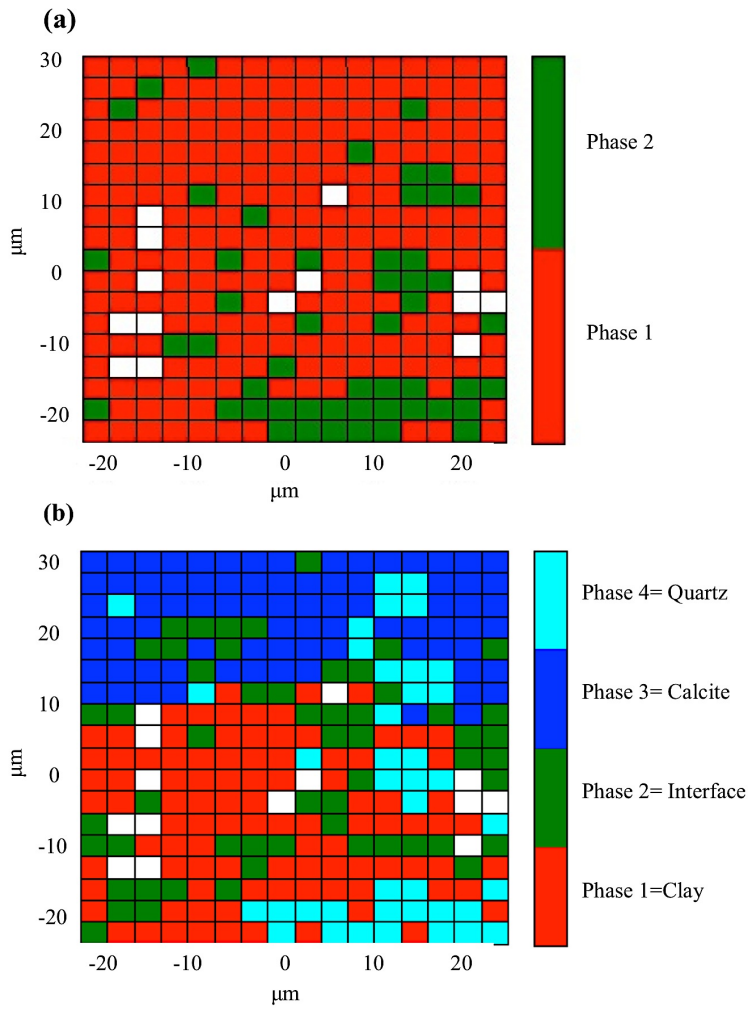

Figure 6. (a) Grid spatial distribution of different material phases detected by clustering analysis of just mechanical data from indentation. White cells represent points with irregular nanoindentation response which are not considered in the analysis. (b) Spatial distribution of different material phases detected by clustering analysis, incorporating both the chemical and mechanical data. [Haynesville].

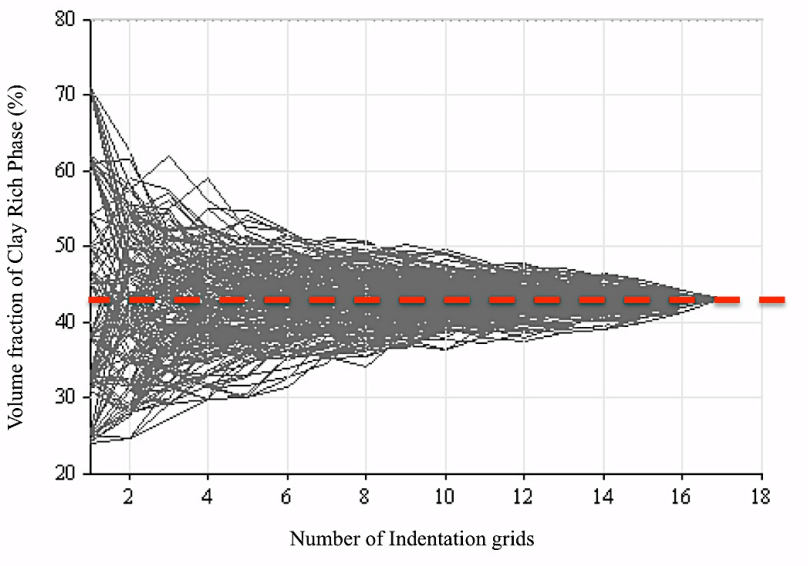

Figure 7. Average volume fraction of clay-rich phase as a function of number of grids. The dashed red line represents the average of all 17 grids.

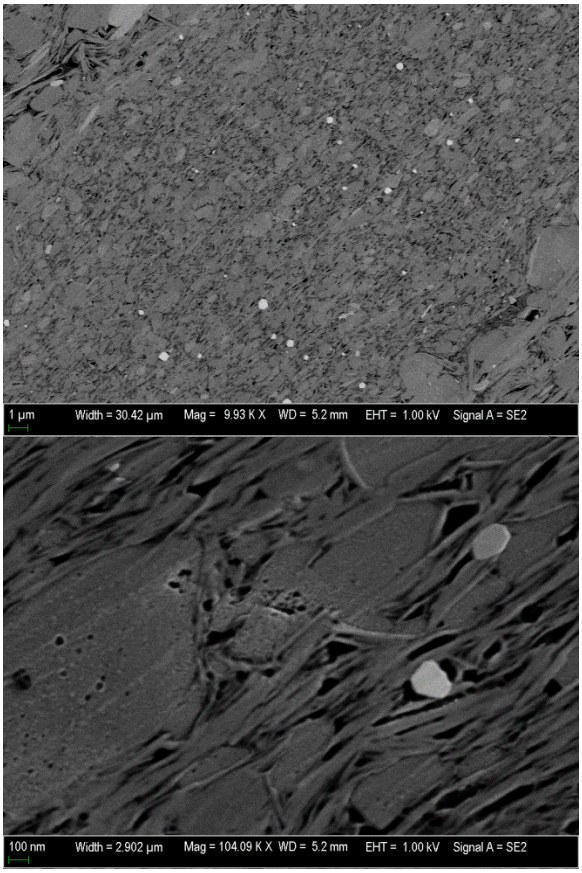

Figure 8. SEM images of Haynesville shale sample at two different magnifications showing the distribution of kerogen in the clay phase.

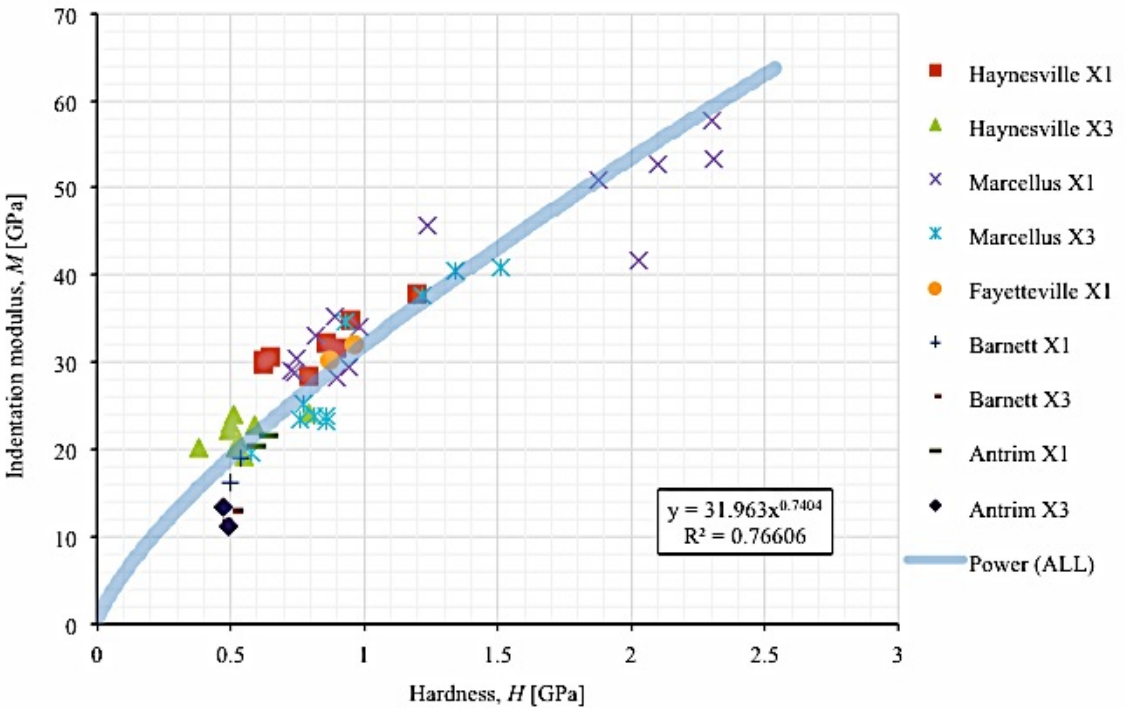

Figure 9. Mean phase properties of clay/kerogen-rich phase: Indentation modulus versus hardness. Haynesville, Marcellus and Fayetteville samples are mature samples, whereas Barnett and Antrim are immature samples. X1 and X3 stand for indentation into the bedding plane and normal-to-bedding plane, respectively.

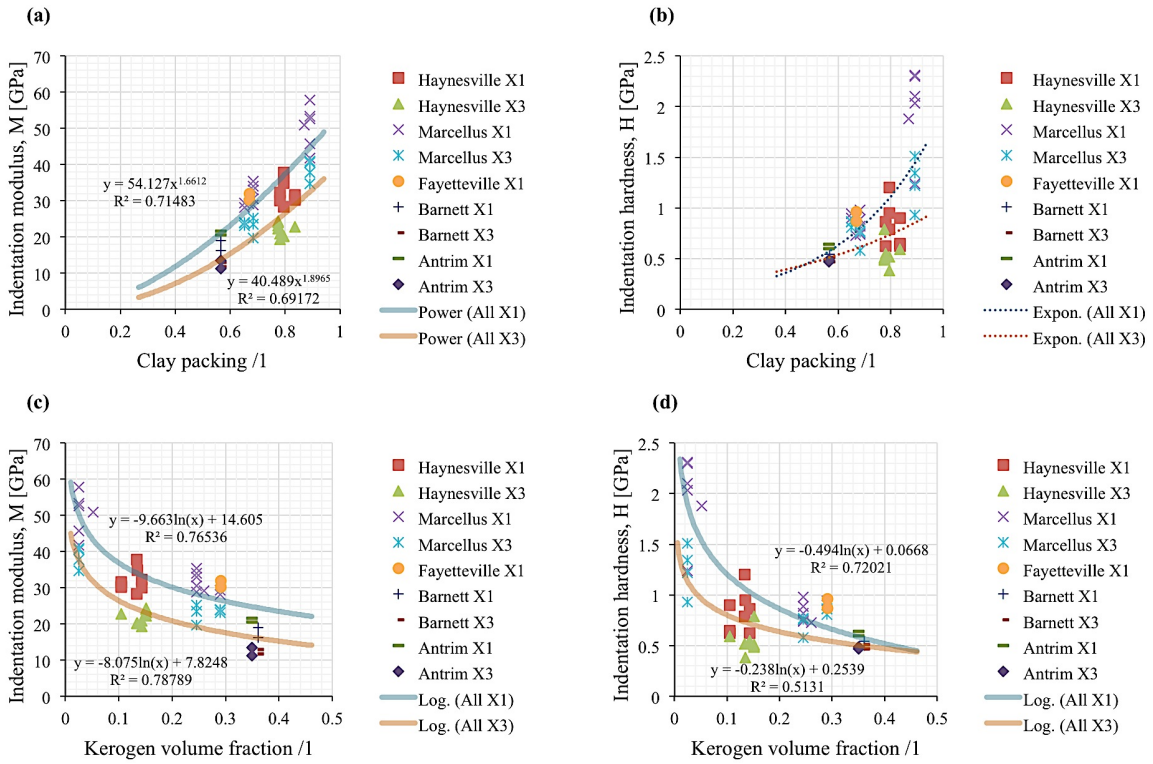

Figure 10. Functional relations between mechanical phase properties (M, H) and (a-b) clay packing density. (c-d) kerogen volume fraction. The kerogen volume fraction η_k was determined from TOC, assuming a constant kerogen density of $\rho_k = 1.2$ g/cc and considering that organic matter is mainly concentrated in the clay phase; whereas the clay packing density was obtained from $\eta_c = 1 - (\eta_k + \phi)$, where ϕ is the porosity. Trend lines are to guide the eyes.

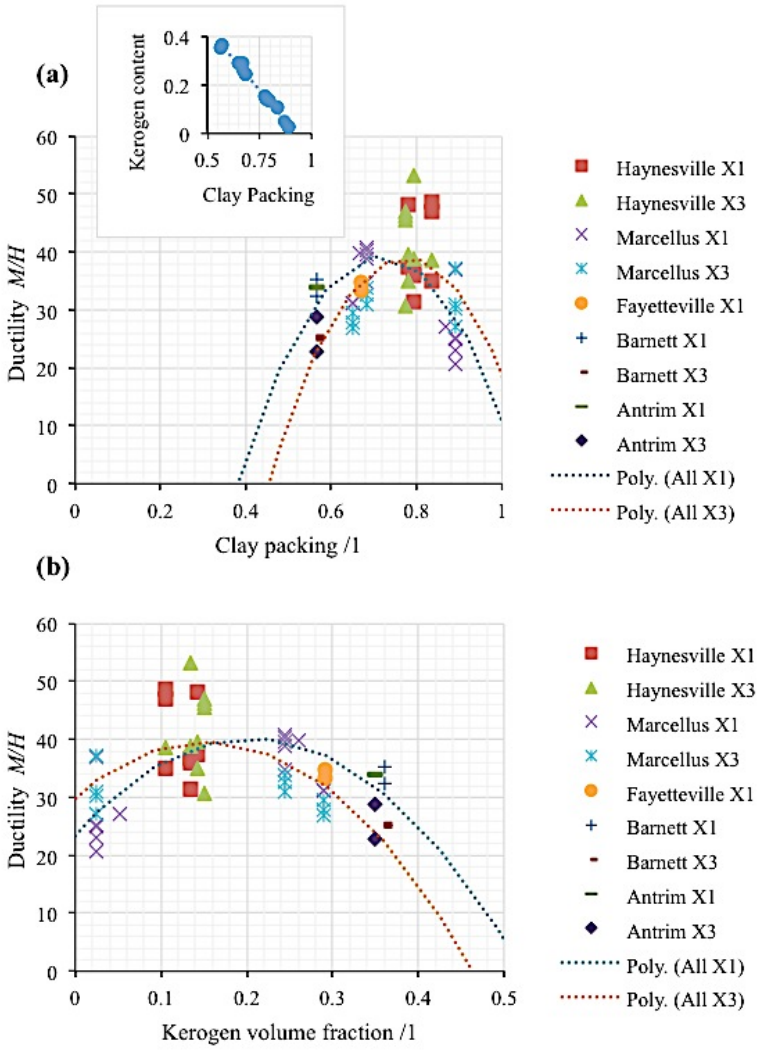

Figure 11. Indentation-modulus-to-hardness ratio vs (a) clay packing, and (b) kerogen content. The kerogen volume fraction η_k was determined from TOC, assuming a constant kerogen density of $\rho_k = 1.2$ g/cc and considering that organic matter is mainly concentrated in the clay phase; whereas the clay packing density was obtained from $\eta_c = 1 - (\eta_k + \phi)$, where ϕ is the porosity. The inlet shows the crossplot of η_k vs. η_c. Trend lines are to guide the eyes. X1 and X3 stand for indentation into the bedding plane and normal-to-bedding plane, respectively.

816 Table 1. Mineralogy, porosity and TOC measurements of the studied samples[a]
817

Sample group	Clay (mass%)	Quartz (mass%)	Carbonates (mass%)	TOC (wt. %)	Porosity (%)
Haynesville	38-45	27-32	9-22	2.6-3.3	6-7.6
Marcellus1	38.9-39.9	18.7-19.7	35.5-37	0.5-1	7.9-8.4
Marcellus2	41.2-48.6	29.4-36.2	4.8-16.1	7.32-8.18	5.9-7.2
Fayetteville	25.1	28.8	31.7	4.9	4
Barnett	41.8	29.7	2.6	12.2	7.3
Antrim	31.41	40.9	4.4	9.6	8.8

818 [a]The mineralogy data were obtained by XRD (courtesy of Shell).
819
820 Table 2. Volume fraction of different material phases present in the studied samples.
821

Sample group	Clay (vol.%)	Quartz (vol.%)	Carbonates (vol.%)	Kerogen (vol.%)
Haynesville	33.1-39.9	23.5-28.1	7.7-18.7	5-6.4
Marcellus1	35.4-36.5	17.3-18.4	32-33.1	1-2.1
Marcellus2	34.1-40.1	24.8-30.4	3.8-13.1	13.6-15.2
Fayetteville	22.7	26.1	27.6	9.85
Barnett	33.4	23.9	2.1	21.4
Antrim	24.5	34.4	3.4	16

822
823
824 Table 3. Volume fraction of kerogen in the clay-rich phase of the studied samples.
825

Sample	Haynesville	Marcellus-1	Marcellus-2	Fayetteville	Barnett	Antrim
η_k	10.5-15	2.5-5.2	24.3-28.8	29.1	34.4	32

826
827
828
829
830
831
832
833
834
835
836

Table 4. Summary of the indentation results of clay/kerogen phases in all studied samples[b] μ, σ, and f_c correspond to the mean value, standard deviation, and surface fraction of the clay-rich/kerogen phase.

Grid number	Number of indents in the grid	M^{μ} [GPa]	M^{σ} [GPa]	H^{μ} [GPa]	H^{σ} [GPa]	$f_c(\%)$
Haynesville-X1-1	362	30.58	7.09	0.65	0.20	25
Haynesville-X1-2	409	30.20	5.43	0.62	0.14	38
Haynesville-X1-3	420	31.60	4.51	0.90	0.17	54
Haynesville-X1-4	419	28.36	6.89	0.79	0.33	33
Haynesville-X1-5	280	37.79	5.00	1.20	0.20	24
Haynesville-X1-6	426	34.90	6.14	0.95	0.20	38
Haynesville-X1-7	381	29.94	7.05	0.62	0.25	47
Haynesville-X1-8	416	32.24	6.56	0.86	0.23	38
Haynesville-X3-1	286	22.85	7.75	0.59	0.26	71
Haynesville-X3-2	412	20.20	5.61	0.38	0.15	38
Haynesville-X3-3	435	20.17	5.43	0.52	0.20	45
Haynesville-X3-4	404	20.94	5.92	0.53	0.23	61
Haynesville-X3-5	396	19.28	4.84	0.55	0.24	62
Haynesville-X3-6	167	23.11	6.17	0.50	0.19	45
Haynesville-X3-7	467	22.32	6.42	0.49	0.26	32
Haynesville-X3-8	327	24.33	4.12	0.79	0.18	50
Haynesville-X3-9	346	24.02	6.54	0.51	0.22	31
Marcellus1-X1-1	447	45.74	9.81	1.24	0.51	34
Marcellus1-X1-2	402	41.70	6.32	2.03	0.57	36
Marcellus1-X1-3	363	53.37	7.32	2.31	0.66	32
Marcellus1-X1-4	423	52.61	7.83	2.10	0.78	23
Marcellus1-X1-5	429	57.70	7.12	2.30	0.40	48
Marcellus1-X1-6	435	50.94	9.01	1.88	0.60	36

[b] μ, σ, and f_c correspond to the mean value, standard deviation, and surface fraction of the clay-rich/kerogen phase.

Table 4 continue. Summary of the indentation results of clay/kerogen phases in all studied samples[b]

Grid number	Number of indents in the grid	M^{μ} [GPa]	M^{σ} [GPa]	H^{μ} [GPa]	H^{σ} [GPa]	$f_c(\%)$
Marcellus1-X3-1	402	34.59	8.31	0.93	0.40	30
Marcellus1-X3-2	318	40.95	9.61	1.51	0.63	49
Marcellus1-X3-3	368	37.74	6.41	1.22	0.51	19
Marcellus1-X3-4	369	40.50	8.11	1.34	0.62	24
Marcellus2-X1-1	366	28.81	5.04	0.74	0.18	66
Marcellus2-X1-2	362	35.30	6.39	0.89	0.18	48
Marcellus2-X1-3	360	33.02	5.76	0.82	0.15	49
Marcellus2-X1-4	368	30.52	5.59	0.75	0.16	44
Marcellus2-X1-5	331	34.06	7.23	0.98	0.27	39
Marcellus2-X1-6	363	29.10	5.55	0.73	0.15	37
Marcellus2-X1-7	371	28.17	5.39	0.90	0.21	50
Marcellus2-X1-8	369	29.41	5.50	0.94	0.18	51
Marcellus2-X3-1	383	19.66	3.44	0.58	0.12	34
Marcellus2-X3-2	407	25.17	4.48	0.77	0.19	47
Marcellus2-X3-3	354	23.51	4.24	0.76	0.16	51
Marcellus2-X3-4	371	23.85	6.22	0.81	0.29	57
Marcellus2-X3-5	390	23.92	5.28	0.86	0.23	53
Marcellus2-X3-6	381	23.19	5.51	0.86	0.29	36
Fayetteville-X1-1	383	31.99	5.91	0.96	0.21	56
Fayetteville-X1-2	389	30.27	6.05	0.87	0.18	30

[b] μ, σ, and f_c correspond to the mean value, standard deviation, and surface fraction of the clay-rich/kerogen phase.

Table 4 continue. Summary of the indentation results of clay/kerogen phases in all studied samples[b]

Grid number	Number of indents in the grid	M^{μ} [GPa]	M^{σ} [GPa]	H^{μ} [GPa]	H^{σ} [GPa]	$f_c(\%)$
Barnett-X1-1	471	18.99	4.56	0.54	0.09	31
Barnett-X1-2	475	16.19	3.07	0.50	0.08	41
Barnett-X3-1	466	11.78	2.45	0.47	0.08	47
Barnett-X3-2	461	12.97	1.87	0.51	0.08	31
Antrim-X1-1	479	21.60	5.33	0.64	0.13	41
Antrim-X1-2	475	20.49	3.58	0.60	0.10	33
Antrim-X3-1	402	13.49	3.06	0.47	0.11	43
Antrim-X3-2	354	11.16	2.40	0.49	0.12	36

[b] μ, σ, and f_c correspond to the mean value, standard deviation, and surface fraction of the clay-rich/kerogen phase.

accounts for inorganic elements. That is, the phases thus identified will certainly include the organic phases as well."

REVIEW: What are the clay mineral types in the different samples?

- AUTHORS' REPLY: Clay minerals in these samples were mostly either illite or mixed illite-smectite, with relatively smaller amounts of kaolinite and chlorite.
- ACTION TAKEN: We have added the above sentence to the revised version of the manuscript for clarification.

REVIEW:
- How did the authors determine dry bulk density?
- drying oil window samples will drive out S1 hydrocarbons
- Is dry density with or without clay-bound waters? Haynesville rocks have considerable amounts of swelling clays: heating temperature will play a big role.

- AUTHORS' REPLY: The temperature that was used for drying the samples was 60° C which is much lower that the temperature that causes the evaporation of clay-bound water and also extraction of S1 hydrocarbons. The above claim is supported by the following references:
- Killops, S., Killops, V. (2005) "Introduction to organic geochemistry" Blackwell Publishing, Malden, MA.
- Saeedi, A. (2012) "Experimental Study of Multiphase Flow in Porous Media during CO2 Geo-Sequestration Processes" Springer Thesis Series, Heidelberg, Germany, Springer Publishing.

REVIEW: Need Rock-eval data or another measure of the produced and trapped hydrocarbons.

- AUTHORS' REPLY: Our Rock-eval data does not provide the amount of produces and hydrated hydrocarbons. However, since the focus of the paper is nanomechanics of porous clay/kerogen phases, the role of produced and trapped hydrocarbons is considered minor compared to TOC, porosity, volume fraction of clay, and state of maturity.

REVIEW: The assumption of kerogen only being associated with clay minerals is not justified.

- AUTHORS' REPLY: This assumption is supported by several papers such as Vernik and Nur, 1992; Kuila et al., 2014, and Fitzgerald et al., 1989.
- ACTION TAKEN: We have added these citations to the revised version of the manuscript. Moreover, Figure 8 in the revised version of the manuscript